Journal of Materials Chemistry C

PAPER

View Article Online
View Journal | View Issue

Cite this: J. Mater. Chem. C, 2015, 3, 4910

Near infrared-emitting tris-bidentate Os(II) phosphors: control of excited state characteristics and fabrication of OLEDs†

Jia-Ling Liao,[a] Yun Chi,*[a] Chia-Chi Yeh,[b] Hao-Che Kao,[b] Chih-Hao Chang,*[b] Mark A. Fox,[c] Paul J. Low*[d] and Gene-Hsiang Lee[e]

Received 21st January 2015,
Accepted 11th April 2015

DOI: 10.1039/c5tc00204d

www.rsc.org/MaterialsC

A series of four Os(II) complexes bearing (i) chromophoric diimine ligands (N^N), such as 2,2′-bipyridine (bpy) and substituted 1,10-phenanthrolines, (ii) dianionic bipz chelate ligands derived from 5,5′-di(trifluoromethyl)-2*H*,2′*H*-3,3′-bipyrazole ($bipzH_2$), and (iii) bis(phospholano)benzene (pp2b) as the third ancillary ligand completing the coordination sphere were synthesized. X-ray diffraction studies confirm the heteroleptic tris-bidentate coordination mode. These Os(II) complexes [Os(N^N)(bipz)(pp2b)], N^N = bpy (**3**), phenanthroline (**4**), 3,4,7,8-tetramethyl-1,10-phenanthroline (**5**) and 4,7-diphenyl-1,10-phenanthroline (**6**), display near infrared (NIR) emission between 717 nm and 779 nm in the solid state at RT. On the basis of hybrid-DFT and TD-DFT calculations, the emissions are assigned to metal-to-ligand charge transfer transitions (^{3}MLCT) admixed with small ligand-to-ligand charge transfer (^{3}LLCT) contributions. Successful fabrication of organic light emitting diodes (OLEDs) using Os(II) complex **5** as the dopant and either tris(8-hydroxyquinoline) aluminum (Alq_3) or 3,3′,5,5′-tetra[(*m*-pyridyl)-phen-3-yl]-biphenyl (BP4mPy) as the host is reported. These OLEDs were measured with emission maxima at 690 nm and extending into the NIR, with peak power efficiencies of up to 0.13 lm W^{-1} and external quantum efficiencies of up to 2.27%.

Introduction

Phosphorescent metal complexes have been extensively investigated during the past two decades due to the profound interest in basic photophysics[1–9] and applications in organic light emitting diodes (OLEDs) suited for the fabrication of flat panel displays[10–13] and luminaires.[14–19] As a consequence of the need for these applications, many studies have focused on achieving bright visible emission, with colors spanning from blue and green to red. Another class of compounds being of great interest is near infrared (NIR) emitting materials; *i.e.* those with emission peak maximum exceeding 700 nm.[20–22] NIR-emitting materials can find application in biological imaging, sensing and optical tele-communication platforms. Among the various systems explored to date, Pt(II) complexes constitute a class of molecules that have shown the most efficient NIR emission,[23–27] either through the use of chelating ligands with extended peripheral π-conjugation or by engineering strong π–π stacking interactions among molecules in the solid state for excimer formation. For example, electroluminescence with peak maximum at 772 nm and an external quantum efficiency (EQE) of 5.0% was documented for Pt(II) tetraphenyltetrabenzoporphyrin,[28] while the maximum EQE was further improved to 9.2% through the introduction of the 3,5-di-*tert*-butylphenyl substituted tetrabenzoporphyrin to control intermolecular interactions and suppress triplet–triplet annihilation.[29]

However, promising results in the area of NIR-emitting materials are not restricted to Pt(II) complexes, and both Ru(II) complexes with π-bonded (η^4-) orthoquinone ligands,[30] Ir(III) complexes bearing cyclometalated heteroaromatics,[31–34] or with azabenz-annulated perylene bisimide[35] stand as illustrative examples of other metal-containing NIR-emitting materials. Parallel to this endeavor, we have developed Os(II) phosphors bearing isoquinolinyl azolate chelate ligands, which lower the emission energy gaps and bring emission into the NIR region.[36,37] The two Os(II) complexes [Os(bpy)(dttz)$(CO)_2$] (**1a**) and [Os(bpy)(dttz)-$(PPhMe_2)_2$] (**2**) bearing both the neutral 2,2′-bipyridine (bpy) and dianionic 3,3′-bi-1,2,4-triazolate ($dttz^{2-}$) chelating ligands also serve to demonstrate important molecular design features (Chart 1).

[a] Department of Chemistry and Low Carbon Energy Research Center, National Tsing Hua University, Hsinchu 30013, Taiwan. E-mail: ychi@mx.nthu.edu.tw
[b] Department of Photonics Engineering, Yuan Ze University, Chungli 32003, Taiwan. E-mail: chc@saturn.yzu.edu.tw
[c] Department of Chemistry, Durham University, South Rd, Durham, DH1 3LE, UK
[d] School of Chemistry and Biochemistry, University of Western Australia, 35 Stirling Highway, Crawley, 6009, Western Australia, Australia. E-mail: paul.low@uwa.edu.au
[e] Instrumentation Center, National Taiwan University, Taipei 10617, Taiwan

† Electronic supplementary information (ESI) available. CCDC 1044312 and 1044313. For ESI and crystallographic data in CIF or other electronic format see DOI: 10.1039/c5tc00204d

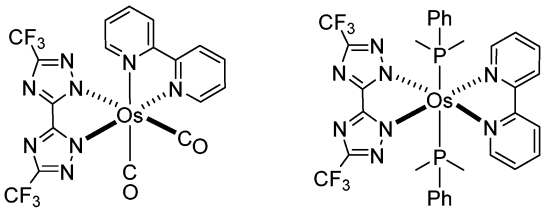

(**1a**) (**2**)

Chart 1 Reported Os(II) complexes **1a** and **2**.

In complex **2** due to the increase in electron density at the Os(II) metal centre brought about by the phosphine co-ligands, we can take advantage of the combined metal-to-ligand charge transfer (MLCT) and the ligand-to-ligand charge transfer (LLCT) transitions to achieve NIR-emitting characteristics.[38]

To further explore the methodology to tune emission into the NIR region, we have designed heteroleptic tris-chelating Os(II) complexes containing (i) bpy or 1,10-phenanthroline as the chelate with lower lying π*-orbitals, (ii) 5,5′-di(trifluoromethyl)-3,3′-bipyrazolate ($bipz^{2-}$) as a dianionic and strongly electron donating chelate, and (iii) 1,2-bis(phospholano)benzene (pp2b) as the third bidentate chelate to impose the formation of all *cis*-coordination geometry. The photophysical and structural characterization of the resulting NIR-emitting Os(II) complexes and the device performance of the NIR-emitting OLEDs formed from these compounds are described here.

Results and discussion

Syntheses and characterization

It has been reported that the cluster complex $Os_3(CO)_{12}$ reacts with functional pyrazoles (or triazoles) to form isolable intermediate derivatives *via* CO elimination.[39–43] Subsequent sequential addition of Me_3NO and phosphines at elevated temperature led to the formation of mononuclear Os(II) complexes with diverse structures and distinctive photophysical properties. Such synthetic procedures were employed to prepare the aforementioned complexes *cis*-[Os(bpy)(dttz)$(CO)_2$] (**1a**) and phosphine substituted *trans*-[Os(bpy)(dttz)$(PMe_2Ph)_2$] (**2**).[38]

Here, this synthetic procedure was extended through reactions of $Os_3(CO)_{12}$ with the distinctive dipyrazole pro-ligand 5,5′-di(trifluoromethyl)-2*H*,2′*H*-3,3′-bipyrazole ($bipzH_2$) and a range of diimine chelates (N^N = bpy, phenanthroline (phen), 3,4,7,8-tetramethyl-1,10-phenanthroline (Me_4phen), and 4,7-diphenyl-1,10-phenanthroline (Ph_2phen)) to give *cis*-[Os(bipz)(N^N)$(CO)_2$] (isolated by way of example for N^N = bpy, **1b**). Further reaction with anhydrous Me_3NO and 1,2-bis(phospholano)benzene (pp2b) gave the tris-heteroleptic complexes [Os(bipz)(N^N)(pp2b)] (**3–6**) (Chart 2).

However, the synthetic yields for **3–6** (21–35%) are notably lower than that obtained for the *trans*-complex **2** (~50%). Varying the *cis*-diphosphine, such as to 1,2-diphenylphosphinobenzene, failed to afford any isolable product, which is in contrast to previous reactions,[44] showing the delicate balance of structural and electronic effects imposed by the phosphines.

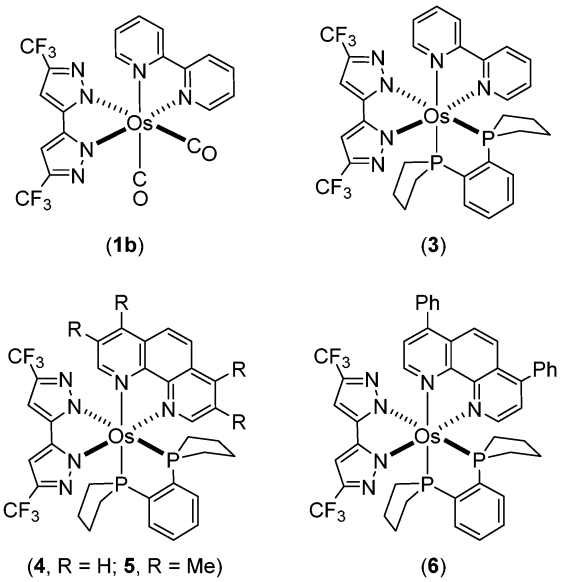

(**1b**) (**3**) (**4**, R = H; **5**, R = Me) (**6**)

Chart 2 Os(II) complexes **1b** and **3–6** investigated in this study.

All of the new Os(II) metal complexes, *i.e.* **1b** and **3–6**, were purified by silica gel column chromatography and recrystallization, and then fully characterized by mass spectrometry, IR and NMR spectroscopies and elemental analyses. Multinuclear NMR spectra clearly established the heteroleptic nature of the complexes; for example, complex **3** showed two distinctive ^{1}H NMR singlet signals at δ 6.54 and 6.39 and two ^{19}F NMR signals at δ −59.62 and −59.65 assigned to the bipz chelate, characteristic multiplets from the bpy ligand, and two well separated ^{31}P NMR signals at δ 39.88 and 33.80 due to the coordinated pp2b ligand. Therefore, these data clearly confirmed the presence of the three distinct chelating ligands coordinated to the Os(II) atom. Moreover, the IR ν(CO) bands of the dicarbonyl complex **1b** were found at 1978 and 2040 cm^{-1}, which are located at lower wavenumbers than those of **1a** (*i.e.* 1994 and 2058 cm^{-1}) which contains the bis(triazolate) ligand, dttz.[38] This observation is in agreement with the greater electron donating character of bipz, and the increased back π-bonding which serves to reduce the CO stretching frequencies.

The structures of **1b** and **3** were determined by single crystal X-ray diffraction, for which a perspective view of each molecule, selected bond distances and angles are shown in Fig. 1 and 2. Both Os(II) complexes adopt a distorted octahedral geometry at the metal centre, with the bpy and bipz chelates being located *cis* to each other, leaving two remaining *cis*-coordination sites that are occupied by two CO ligands (**1c**) or the pp2b chelate (**3**). In complex **1b**, the *trans*-influence of the CO ligands increases the *trans*-Os–N distances (*i.e.* Os–N(2) = 2.102(4) and Os–N(6) = 2.121(4) Å) *versus* those at the *cis*-dispositions, *cf.* Os–N(3) = 2.057(4) and Os–N(5) = 2.080(4) Å.[39] For the pp2b complex **3**, since both the *trans*-Os–N distances, *i.e.* Os–N(3) = 2.113(6) and Os–N(6) = 2.123(5) Å, are comparable to the *trans*-Os–N distances observed in **1c**, the *trans*-influence of the pp2b chelate should be at the same magnitude as that imposed by dual CO ligands, despite the large distinction in their intrinsic characters, *i.e.* σ-donor *vs.* π-acceptor.[45] Moreover, the bipz chelate in **3** adopts

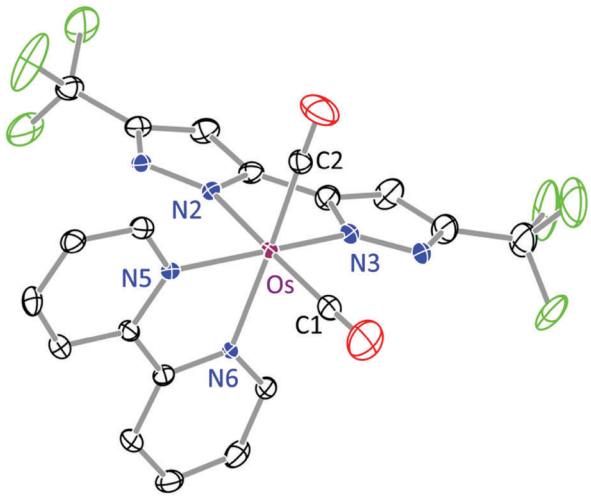

Fig. 1 ORTEP diagram of **1b** with thermal ellipsoids shown at the 30% probability level; selected bond distances: Os–N(2) = 2.102(4), Os–N(3) = 2.057(4), Os–N(5) = 2.080(4), Os–N(6) = 2.121(4), Os–C(1) = 1.892(6) and Os–C(2) = 1.895(6) Å; bond angles: ∠C(1)–Os–C(2) = 87.8(2), N(5)–Os–N(6) = 77.94(16) and N(2)–Os–N(3) = 76.85(17)°.

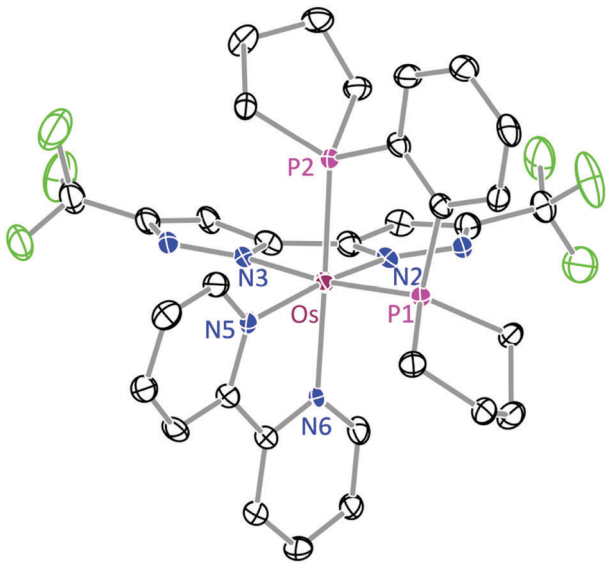

Fig. 2 ORTEP diagram of **3** with thermal ellipsoids shown at the 30% probability level; selected bond distances: Os–N(2) = 2.088(5), Os–N(3) = 2.113(6), Os–N(5) = 2.072(6), Os–N(6) = 2.123(5), Os–P(1) = 2.2650(17) and Os–P(2) = 2.2618(17) Å; bond angles: ∠P(1)–Os–P(2) = 85.36(6), N(5)–Os–N(6) = 77.1(2) and N(2)–Os–N(3) = 76.2(2)°.

a subtly bent conformation, which is in contrast to the near-planar arrangement of this ligand in **1b**. Since pp2b is more sterically bulky than the CO ligands, the associated crystal-packing effect, in part, likely influences this conformational distortion in the crystal lattice.[46]

Photophysical data

Complex **1b** is non-emissive in both solution and solid states, so the discussion of photophysical properties is focused only on the phosphine substituted Os(II) complexes **3–6**. For these complexes, UV-Vis absorption spectra were recorded in CH_2Cl_2 and the numerical data are presented in Table 1. As shown in Fig. 3, the absorption spectra exhibit strong absorption bands below 320 nm ($\varepsilon > 3 \times 10^4$ $M^{-1}cm^{-1}$) assigned to $^1\pi$–π^* transitions localized on the diimine ligands. The next lower energy absorption in the region 400–500 nm (ε = 4–10 $\times$ 10^3 $M^{-1}cm^{-1}$) is attributed to the spin-allowed ^{1}MLCT transitions from the Os(II) metal ion to the diimine. The intensities of these ^{1}MLCT bands show strong correlation with the nature of the diimine ligands; *i.e.* complexes **3** and **6** give the weakest and greatest intensity transitions which may be due in part to the degree of π-conjugation in the diimine acceptor. Moreover, there is a very broad absorption envelope that extends beyond 600 nm (ε = 1.2–2.1 $\times$ 10^3 M^{-1} cm^{-1}), which can be assigned to the heavy-metal atom enhanced ^{3}MLCT absorption, probably mixed with a contribution from the ligand-to-ligand charge transfer (^{3}LLCT) transitions from the occupied orbital of bipz to the empty π*-orbital of the diimine chelate.

The Os(II) complexes **3–6** failed to show any notable emission in solution at RT, but were significantly emissive in the solid state, a result of the rigid media as well as the forfeit of solvent collisions.[47,48] The solid state emission spectra and associated peak maxima (Fig. 3) are sensitive to the nature of the diimine N^N chelate, supporting the assignment of the ^{3}MLCT transition. For example, replacing the bpy chelate in **3** with the phen chelate in **4** leads to a blue shift of emission from 772 nm to 739 nm, which is due to the more destabilized π*-orbital of phen *versus* bpy.[49–52] In a similar fashion, upon introduction of four methyl substituents (**5**) or two phenyl groups (**6**) into the phenanthroline ligand, the corresponding emission maxima are blue shifted relative to the parent complex **4** to 717 nm and red shifted to 779 nm, respectively. These variations are attributed to the electron donating and extended π-conjugation of the methyl and phenyl substituents respectively.

Complexes **3–6** showed emission quantum yields Φ = 0.5–8.8%, and relatively short luminescence lifetimes at RT (τ_{obs} = 26.4–431 ns) for phosphorescence processes. The radiative (k_r) and nonradiative decay (k_{nr}) rates were calculated from the Φ and τ data. The low Φ value of **3** is principally caused by the less

Table 1 Photophysical properties of the NIR-emitting Os(II) complexes **3–6**

	Abs. λ_{max} (nm) [ε (10^3 M^{-1} cm^{-1})][a]	PL λ_{max}[b] (nm)	Φ[b] (%)	τ_{obs}[b] (ns)	k_r (10^5 s^{-1})	k_{nr} (10^7 s^{-1})
3	295 [27.9], 338 [5.4], 471 [4.1], 610 [1.2]	772	0.5	26.4	1.89	3.76
4	268 [43.0], 406 [6.1], 586 [1.2]	739	3.1	197	1.52	0.49
5	273 [57.4], 442 [6.9], 545 [1.7]	717	8.8	431	2.04	0.21
6	279 [64.2], 476 [10.3], 599 [2.1]	779	4.5	115	3.91	0.83

[a] UV-Vis spectra were recorded in 10^{-5} M of CH_2Cl_2 solution. [b] Photoluminescence spectra and quantum yields were measured as neat powder.

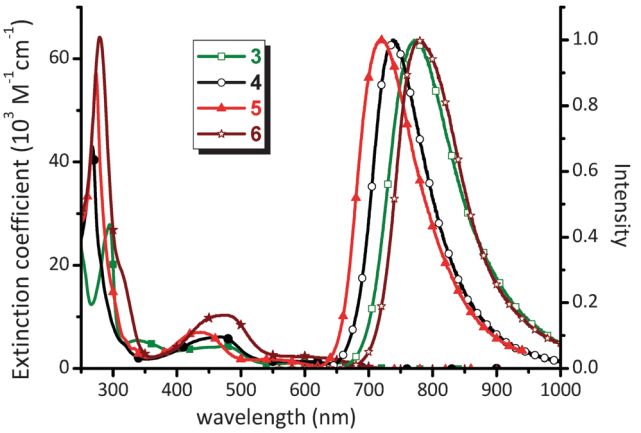

Fig. 3 UV-Vis absorption spectra in CH_2Cl_2 and solid state emission spectra at RT of Os(II) complexes **3–6**.

rigid molecular framework of the bpy ligand, which then increases k_{nr} *versus* other Os(II) complexes with more structurally rigid phenanthroline-based chelates.[53] Within the series of phenanthroline complexes **4–6**, complex **5** showed higher Φ and longer τ_{obs} values *versus* those of parent **4**, which is best explained by the energy gap law,[54,55] *i.e.* k_{nr} values tend to increase as the emission energy decreases. In the case of complex **6** with the extended Ph_2phen chelate, the Φ value of 4.5% is higher than 3.1% of **4**, whilst τ_{obs} (115 ns) is comparable to that of parent complex **4** (197 ns). The derived k_r and k_{nr} values for **6** are calculated to be 3.91×10^5 and 0.83×10^7 s^{-1}, respectively. This could be due to the fact that, upon photoexcitation, the peripheral Ph substituents would become coplanar with the phenanthroline backbone, resulting in more extended electron delocalization in the excited state.[56,57] Therefore, the better electron delocalization produces a smaller variation in the C–C bond lengths upon formation of the excited state as compared to the ground state and, ultimately, giving the larger radiative quantum yield relative to other molecules in this class.[58]

Electrochemistry

The electrochemical properties of **3–6** were examined using cyclic voltammetry (Table 2). The obtained data support the delineation that oxidation is localized on the Os(II) metal center, and that reduction occurs mainly on the diimine ligand.[59] In the present system, all Os(II) complexes **3–6** showed a reversible oxidation potential in the narrow range of 0.00–0.07 V (*vs.* the ferrocenium/ferrocene couple at 0.0 V), whilst the reduction potential was recorded between −2.04 and −2.30 V (*cf.* Table 2 and Fig. S1 of the ESI†). The trends in reduction potentials followed the trends anticipated on the basis of the electron donating or withdrawing characteristics of the diimine ligands. Thus, changing from bpy to phen (*i.e.* from **3** to **4**) and addition of four methyl groups to phen (*i.e.* from **4** to **5**) result in the destabilization of the empty π*-orbital of the diimine chelate, and a consequent shift in the reduction potential to more negative values. For **5**, the small decrease in oxidation potential *versus* **4** is also coupled with the increase in electron density at the metal center exerted by four methyl groups on phen. The possibility to create a more extended π* system in the Ph_2phen complex **6** gives the least negative reduction potential when compared with the parent compound **4**.

Table 2 Electrochemical properties of the studied Os(II) complexes

	Ox. $E_{1/2}$[a] (V) [ΔE_p (mV)]	Red. $E_{1/2}$[b] (V) [ΔE_p (mV)]		HOMO[c] (eV)	LUMO[c] (eV)
3	0.07 [89]	−2.14 [124]	**3′**	−5.00	−2.16
4	0.07 [99]	−2.22 [83]	**4′**	−5.00	−2.13
5	0.00 [88]	−2.30 [73]	**5′**	−5.03	−1.91
6	0.07 [72]	−2.04 [73]	**6′**	−4.98	−2.18

[a] Measured in 0.1 M $TBAPF_6/CH_2Cl_2$ *vs.* FcH^+/FcH with the Pt working electrode. [b] Measured in 0.1 M $TBAPF_6$/THF *vs.* FcH^+/FcH with the Au working electrode. [c] B3LYP/LANL2DZ:6-31G** data.

DFT calculations

In order to gain in-depth insight into the above experimentally observed properties, we turned to calculations based on density functional theory (DFT) and time-dependent density functional theory (TD-DFT) (B3LYP/LANL2DZ basis set for Os, 6-31G** and all other atoms, as well as a conductor-like polarization continuum CPCM solvent model in CH_2Cl_2). The model structures are denoted **3′**, **4′**, **5′** and **6′** to distinguish them from the physical data of the as-synthesized complexes. The results from the geometry optimisation are summarised in Table 3, together with the crystallographically determined data from **3** for comparison. In the case of **3** and **3′**, the majority of differences in bond lengths are within 0.03 Å, whilst the greatest difference is around 0.06 Å, associated with the Os–P(2) bond.

Plots of the HOMO and the LUMO of **3′**, **4′**, **5′** and **6′** are given in Fig. 4 and the ESI.† In each case, the HOMO is of mixed Os(d)–bipz(π) characteristics, (Os/bipz: 49/44 (**3′**); 48/45 (**4′**); 57/32 (**5′**); 49/44 (**6′**)) whilst the LUMO is strongly localized on the diimine ligand. The HOMO energies vary little across the series (Table 2) whilst the LUMO energies naturally follow the electronic characteristics of the diamine, giving good correlation with the redox potentials.

To provide a more detailed interpretation of the photophysical properties of **3–6**, time-dependent density functional theory (TD-DFT) calculations were also carried out. The results are summarized in Table 4, which lists the energy and orbital analyses of the lowest energy singlet and triplet transitions, together with the relevant data from the absorption and emission spectra.

Table 3 Selected bond lengths (Å) and angles (°) of **3** and the computational models **3′**, **4′**, **5′** and **6′**

	3	**3′**	**4′**	**5′**	**6′**
Os–N(2) (in Å)	2.088(5)	2.1101	2.1077	2.0898	2.1098
Os–N(3)	2.113(6)	2.1346	2.1349	2.1041	2.1353
Os–N(5)	2.072(6)	2.1094	2.1207	2.0909	2.1192
Os–N(6)	2.123(5)	2.1276	2.1387	2.1149	2.1308
Os–P(1)	2.2650(17)	2.3334	2.3312	2.3068	2.3337
Os–P(2)	2.2618(17)	2.3204	2.3174	2.3013	2.3185
P(1)–Os–P(2) (in °)	85.36(6)	84.48	84.63	85.38	84.49
N(2)–Os–N(3)	76.2(2)	75.95	76.05	75.92	75.94
N(5)–Os–N(6)	77.1(2)	76.92	77.71	77.96	77.26

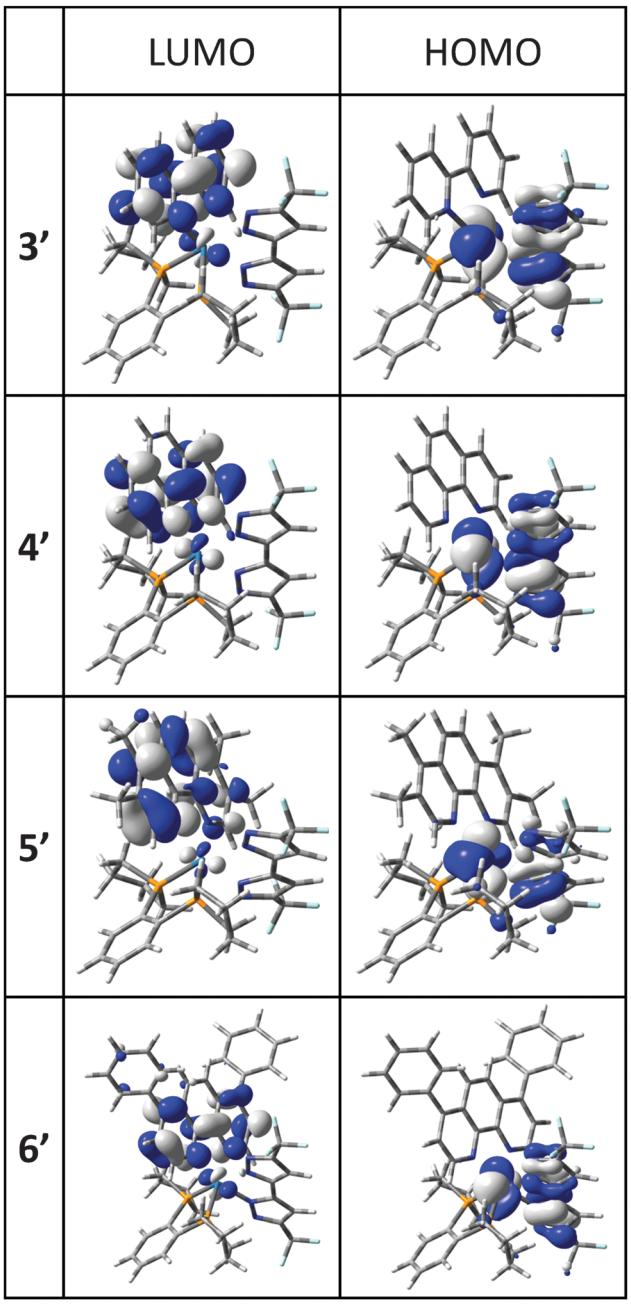

Fig. 4 Frontier molecular orbitals in the lowest-energy optical transitions for Os(II) complexes **3′–6′**; all contours are plotted at ±0.04 (e bohr^{-3})$^{1/2}$.

The agreement between the calculated $S_0 \rightarrow S_1$ transition energies is remarkably good, and although the $S_0 \rightarrow T_1$ transition is strictly forbidden and the calculations do not allow for spin–orbit coupling, the calculated transition energies (albeit with zero oscillator strength) follow the trend in emission maxima (Table 4). The $S_0 \rightarrow T_1$ transition energies may also account in part for the low energy tails observed in the absorption spectra (Fig. 3). The simulated absorption spectra of the Os(II) complexes **3–6** are given in the ESI.†

The $S_0 \rightarrow S_1$ and $S_0 \rightarrow T_1$ transitions are assigned to HOMO → LUMO charge transfer processes of mixed MLCT/LLCT characteristics for each of **3′**, **4′** and **6′**. In the case of **5** which bears the Me_4-phen ligand, the $S_0 \rightarrow S_1$ transition also has appreciable HOMO → LUMO+1 characteristics (also MLCT/LLCT between the Os/bipz donor and the diimine) whilst the $S_0 \rightarrow T_1$ transition is of mixed HOMO−1 → LUMO/HOMO−2 → LUMO characteristics (again, largely MLCT/LLCT in nature).

OLED device fabrication

For OLED device fabrication, complex **5** was selected as the dopant due to both the higher volatility and quantum yield compared with the other members of the series. In this study, tris(8-hydroxyquinoline)aluminum (Alq_3) and 3,3′,5,5′-tetra[(*m*-pyridyl)-phen-3-yl]-biphenyl (BP4mPy) were used both as the host and the electron transport layer (ETL). The electron mobilities of Alq_3 and BP4mPy are found to be 10^{-5} and 10^{-4} cm^2 V^{-1} s^{-1}, respectively.[60–63] Moreover, 4,4′-bis[*N*-(1-naphthyl)-*N*-phenyl-amino] biphenyl (NPB) which possesses an adequate hole transport mobility ($\sim 10^{-4}$ cm^2 V^{-1} s^{-1}) and a triplet energy gap (E_T = 2.29 eV) was selected as the hole transport layer (HTL) in tuning the carrier balance.[64–66] The devices A1 and B1 consist of the architecture: ITO/NPB (40 nm)/Host (Alq_3 or BP4mPy) doped with *x* wt% **5** (30 nm)/ETL (Alq_3 or BP4mPy) (40 nm)/LiF (0.5 nm)/Al (150 nm). In general, the concentrations of all RGB dopants in phosphorescent OLEDs range from 6 to 10 wt%. However, NIR OLEDs usually require higher concentrations to achieve the desired red-shifted EL spectrum; therefore, 8 wt% and 16 wt% concentrations were used here. The EL spectrum from the device with 16 wt% of dopant was slightly red-shifted compared to the EL spectrum from the device with 8 wt% of dopant. However, the device adopting 8 wt% doping concentration achieved a much higher efficiency value. Consequently, the doping concentration of 8 wt% was used in this study. Furthermore, based

Table 4 Calculated $S_0 \rightarrow S_1$ and $S_0 \rightarrow T_1$ transition energies (in nm), orbital analysis and optical properties of **3′**, **4′**, **5′** and **6′**

	Calc. λ_{max}	Calc. λ_{max}		
	$S_0 \rightarrow S_1$	$S_0 \rightarrow T_1$	Obs. λ_{max} (abs)	Obs. λ_{max} (em)
3′	607 HOMO → LUMO (95%)	644 HOMO → LUMO (76%)	610	772
4′	598 HOMO → LUMO (95%)	633 HOMO → LUMO (70%)	586	739
5′	533 HOMO → LUMO (58%) HOMO → LUMO+1 (33%)	596 HOMO-1 → LUMO (52%) HOMO-2 → LUMO (26%)	545	717
6′	608 HOMO → LUMO (93%)	651 HOMO → LUMO (63%)	599	779

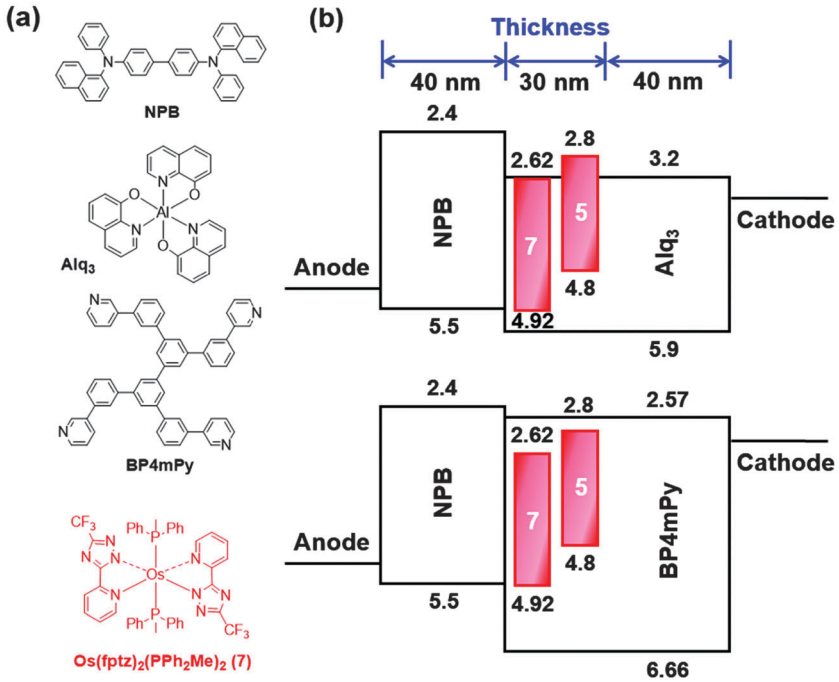

Fig. 5 (a) Compounds used in OLEDs along with complex **5**; (b) architecture of NIR OLEDs with the tested hosts, dopants and electron transport layers.

on our experiences, the device efficiency can be improved by using a second dopant with an intermediate energy level to provide a favorable stepwise energy transfer. The Os(II) complex $[Os(fptz)_2(PPh_2Me)_2]$ (**7**) was selected for this purpose as it exhibited a considerable spectral overlap with that of **5**, as well as the optimal energy levels.[40,67–69] This isoenergetic relationship allows efficient energy transfer from **7** to **5**, and the emission remained unaltered due to the low concentration of **7**.[38,64] Therefore, the doped devices A2 and B2 were represented by the architecture: ITO/ NPB (40 nm)/Host (Alq_3 or BP4mPy)

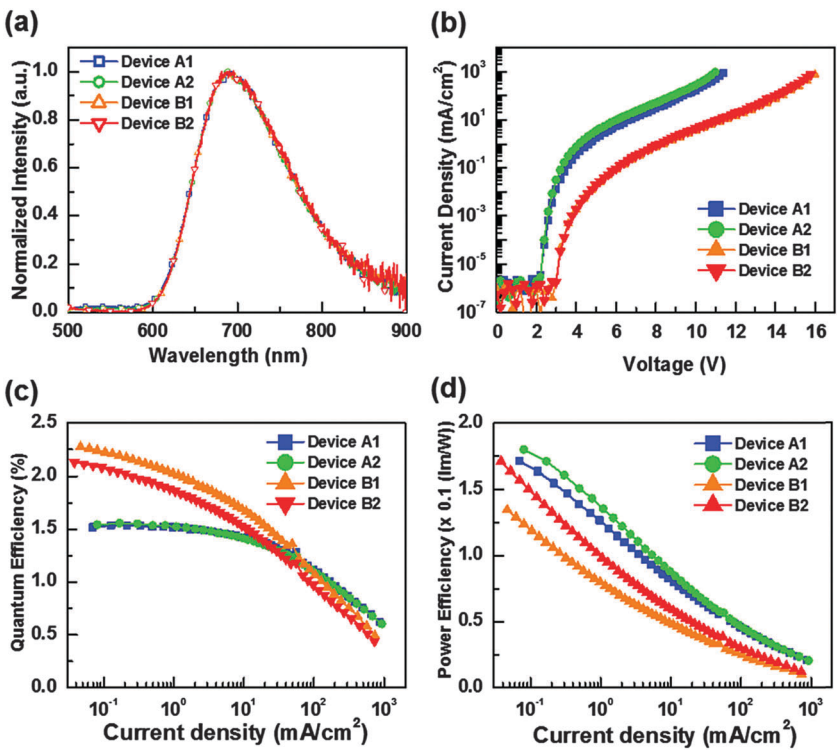

Fig. 6 (a) EL spectra of tested OLEDs; (b) current density–voltage (*J*–*V*) plots; (c) external quantum efficiency *vs.* current density; (d) power efficiency *vs.* current density for devices A1, A2, B1 and B2.

Table 5 EL characteristics of NIR OLEDs with different dopants

Device		A1	A2	B1	B2
Host & ETL		Alq_3		BP4mPy	
Dopant		**5**	**5** + Os	**5**	5 + Os
External quantum efficiency (%)	Max.	1.54	1.56	2.27	2.13
	10 mA cm^{-2}	1.42	1.41	1.68	1.53
Power efficiency (lm W^{-1})	Max.	0.17	0.18	0.13	0.17
	10 mA cm^{-2}	0.08	0.09	0.05	0.06
Turn on voltage (V)		2.2	2.2	3.0	3.0
$J_{1/2}$ (mA cm^{-2})		473.2	441.9	82.3	69.5
CIE 1931 coordinates		(0.66, 0.34)	(0.67, 0.33)	(0.69, 0.31)	(0.69, 0.31)
Light output (mW cm^{-2}) [@V]		53.9 [11.4 V]	52.8 [11.0 V]	48.9 [16.0 V]	45.9 [15.8 V]

doped with 8 wt% **5** and 0.1 wt% **7** (30 nm)/ETL (Alq_3 or BP4mPy) (40 nm)/LiF (0.5 nm)/Al (150 nm). The materials employed in OLEDs along with complex **5** and an estimated energy-level diagram for the devices are depicted in Fig. 5.

The characteristics of the resulting devices are shown in Fig. 6, while the numerical data are listed in Table 5. As can be seen, all devices show nearly identical spectral profiles, for which the EL peak maxima (690 nm) show a broadened full width at half maximum (FWHM) of approx. 130 nm (or 2680 cm^{-1}) and are also slightly blue-shifted with respect to photoluminescence (PL) recorded as neat powder (717 nm). It appears to us that the blue-shifting in EL spectra may be due to the effect of media, for which the co-deposition in host material may somewhat destabilize the ^{3}MLCT excited states. Furthermore, the lack of Alq_3 or BP4mPy emission implies that complete energy transfers take place from the hosts to the NIR dopant **5**. Hence, the carrier recombination zone was confined within the emitting layer and the exciton diffusion to the adjacent carrier transport layers is avoided in the devices.

Moreover, the respective turn-on voltages (defined as a sharp rise in current density) for devices A1, A2, B1, and B2 are found to be 2.2 V, 2.2 V, 3.0 V and 3.0 V, respectively. Obviously, the higher band gap of BP4mPy produced higher operation voltages and lower current densities for devices B1 and B2 *versus* devices A1 and A2 that were fabricated using Alq_3. As shown in Fig. 6(c) and (d), devices A1 and A2 showed poor external quantum efficiencies (EQE) at lower current densities, which might be attributed to the quenching induced by the charge carrier–exciton interaction.[70] Peak EQEs of A1 and A2 were recorded to be 1.54% (0.17 lm W^{-1}) and 1.56% (0.18 lm W^{-1}), respectively. In contrast, the peak EQEs of B1 and B2 were higher, *e.g.* 2.27% (0.13 lm W^{-1}) and 2.13% (0.17 lm W^{-1}), respectively. This approx. 47% increase in EQEs demonstrated the effectiveness of BP4mPy in achieving the balanced carrier transport. On the other hand, both the co-doped devices A2 and B2 showed improved carrier transporting ability and, hence, increased max. power efficiency as compared to those without the co-dopant **7** (*i.e.* A1 and B1).

In addition, the EQEs of devices A1 and A2 (*i.e.* with Alq_3) decreased to one-half of their highest values at a current density ($J_{1/2}$) of 473.2 and 441.9 mA cm^{-2}, and at a $J_{1/2}$ of 82.3 and 69.5 mA cm^{-2} for B1 and B2 (*i.e.* BP4mPy).[71,72] Devices A1 and A2 showed much higher overall current densities because of the reduced efficiency roll-off, which is partially attributed to the lower electron mobility of Alq_3 ($\sim 10^{-5}$ cm^2 V^{-1} s^{-1}). Therefore, the relatively fast hole injection from NPB to Alq_3 enlarged the recombination zone (RZ) and thus decreased the exciton concentration. In contrast, BP4mPy with a higher electron mobility of $\sim 10^{-4}$ cm^2 V^{-1} s^{-1} restrained the thickness of RZ, resulting in a relatively high exciton concentration in a narrow space. The increase in triplet excitons with long excited-state lifetimes would substantially increase the probability of triplet–triplet annihilation as well as triplet polaron quenching.[73–75] As such, devices B1 and B2 only achieved a light output of 48.9 and 45.9 mW cm^{-2} at 16.0 V and 15.8 V. In contrast, a forward light output as high as 53.9 and 52.8 mW cm^{-2} can be reached at lower voltages of 11.4 V and 11.0 V for devices A1 and A2, respectively.

Conclusion

In summary, a new series of NIR-emitting Os(II) phosphors bearing heteroleptic tris-bidentate chelating architecture were synthesized and characterized, among which Os(II) complexes **5** and **6** showed PL emission at 717 nm with Φ = 8.8% and at 779 nm with Φ = 4.5%, respectively in the solid state. Their lower-energy emission is generally derived from the mixed ^{3}MLCT and ^{3}LLCT excited states, while the higher emission efficiencies are, in part, attributed to the higher rigidity of coordinated phenanthroline that reduced the vibronic coupling in the excited states. Hence, a better emission efficiency than predicted by the energy gap law can be achieved.

NIR-emitting OLEDs were fabricated using the highly emissive Os(II) phosphor **5**, giving a peak external quantum efficiency (EQE) of 1.54%, a power efficiency (PE) of 0.17 lm W^{-1}, and a low turn-on voltage of 2.2 V with Alq_3 both as the host and the ETL. In addition, the peak EQE increased to 2.27% by substituting Alq_3 with BP4mPy, due to their better carrier balance and exciton confinement. Overall, these results pinpoint the great potential of the relevant Os(II) phosphors in the fabrication of NIR-emitting OLEDs.

Experimental section

General information and materials

Mass spectra were recorded on a JEOL SX-102A instrument operating in electron impact (EI) mode or fast atom bombardment (FAB) mode. ^{1}H, ^{19}F and ^{31}P NMR spectra were obtained

using the Varian Mercury-400 or INOVA-500 instruments. Elemental analyses were performed in the NSC Regional Instrumentation Center at National Chao Tung University, Hsinchu, Taiwan. 5,5′-Di(trifluoromethyl)-2*H*,2′*H*-3,3′-bipyrazole ($bipzH_2$) was prepared according to the literature procedure.[76] All reactions were carried out under N_2 atmosphere and anhydrous conditions.

Photophysical measurement

Steady-state absorption and emission spectra were recorded using a Hitachi (U-3900) spectrophotometer and an Edinburgh (FLS920) fluorimeter, respectively. The quantum yield (Q.Y.) of each complex in the solid was measured using an integrating sphere,[77,78] which has been calibrated by wavelength response and incorporated into the aforementioned fluorimeter, to obtain the absolute emission yield.

Cyclic voltammetry

All electrochemical potentials were measured in a 0.1 M $TBAPF_6/CH_2Cl_2$ and THF solution for oxidation and reduction reactions, and reported in volts using FcH/FcH^+ as the reference; ΔE_p is defined as E_{ap} (anodic peak potential) − E_{cp} (cathodic peak potential) and these data are reported in mV. The Pt electrode and the Au(Hg) alloy were selected as the working electrode for oxidation and reduction processes, respectively.

Preparation of 1b

A mixture of $Os_3(CO)_{12}$ (100 mg, 0.11 mmol), $bipzH_2$ (93 mg, 0.34 mmol) and bipyridine (bpy, 53 mg, 0.340 mmol) in diethylene glycol monomethyl ether (DGME, 10 mL) was heated to 190 °C for 24 h. After cooling to RT, the solvent was removed under vacuum. The residue was purified by silica gel column chromatography eluting with ethyl acetate (EA) : hexane (2 : 1), followed by recrystallization of a mixture of EA and hexane, giving a yellow solid (**1b**, 141 mg, 0.21 mmol, 63%).

Spectroscopic data of 1b

^{1}H NMR (400 MHz, d_6-acetone, 294 K): δ 9.47 (dd, J = 5.6, 0.8 Hz, 1H), 8.76 (d, J = 8.4 Hz, 1H), 8.69 (d, J = 8.4 Hz, 1H), 8.45 (td, J = 8.0, 0.8 Hz, 1H), 8.29 (td, J = 8.0, 0.8 Hz, 1H), 7.88 (td, J = 6.8, 0.8 Hz, 1H), 7.68 (td, J = 6.8, 0.8 Hz, 1H), 7.37 (d, J = 6.8 Hz, 1H), 6.70 (s, 1H), 6.48 (s, 1H); ^{19}F–{^{1}H} NMR (470 MHz, d_6-acetone, 294 K): δ −60.62 (s, 3F), −60.84 (s, 3F); MS (FAB, ^{192}Os): m/z 672 $(M–2)^+$, 645 $(M^+–CO)$, 616 $(M^+–2CO)$; IR (CH_2Cl_2): ν(CO), 1978 (s), 2040 (s) cm^{-1}; anal. calcd for $C_{20}H_{10}F_6N_6O_2Os$: N, 12.53; C, 35.82; H, 1.50. Found: N, 12.17; C, 35.62; H, 1.94.

Selected crystal data of 1b

$C_{44}H_{28}F_{12}N_{12}O_6Os_2$; M = 1429.18; triclinic; space group = $P\bar{1}$; a = 10.1401(7) Å, b = 14.5567(10) Å, c = 17.5318(12) Å, α = 82.8000(14)°, β = 79.8955(15)°, γ = 83.7633(15)°, V = 2517.6(3) Å^3; Z = 2; ρ_{calcd} = 1.885 Mg m^{-3}; F(000) = 1368; crystal size = 0.40 × 0.40 × 0.25 mm^3; λ(Mo-K$_\alpha$) = 0.71073 Å; T = 150(2) K; μ = 5.145 mm^{-1}; 29 504 reflections collected, 11 522 independent reflections (R_{int} = 0.0358), GOF = 1.061, final $R_1[I > 2\sigma(I)]$ = 0.0353 and wR_2 (all data) = 0.1026.

Preparation of 3

A mixture of $Os_3(CO)_{12}$ (100 mg, 0.11 mmol), $bipzH_2$ (93 mg, 0.34 mmol) and bpy (53 mg, 0.34 mmol) in 10 mL of DGME was heated to 190 °C for 24 h. After the reaction mixture was cooled to RT, freshly sublimed Me_3NO (52 mg, 0.69 mmol) was added and the solution was then heated to 110 °C for 1 h. After that 1,2-bis(phospholano)benzene (pp2b, 91 mg, 0.36 mmol) was added into the solution and then heated to 190 °C for 12 h. Finally, the solvent was removed under vacuum, and the residue was purified by silica gel column chromatography eluting with EA : hexane (2 : 1). Recrystallization of a mixture of EA and hexane gave a dark-brown crystalline solid (90 mg, 0.10 mmol, 31%).

Spectroscopic data of 3

^{1}H NMR (400 MHz, d_6-acetone, 294 K): δ 8.65 (d, J = 5.6 Hz, 1H), 8.41 (d, J = 8.0 Hz, 2H), 7.87 (m, 3H), 7.79 (m, 2H), 7.50 (m, 2H), 7.37 (t, J = 6.4 Hz, 1H), 7.17 (t, J = 6.4 Hz, 1H), 6.54 (s, 1H), 6.39 (s, 1H), 3.61 (m, 1H), 2.62 (m, 1H), 2.47 (m, 1H), 2.15 (m, 1H), 1.80 (m, 3H), 1.68 (m, 1H), 1.27 (m, 5H), 0.77 (m, 3H); ^{19}F–{^{1}H} NMR (470 MHz, d_6-acetone, 294 K): δ −59.62 (s, 3F), −59.65 (s, 3F); ^{31}P NMR (202 MHz, d_6-acetone, 298 K): δ 39.88 (s, 1P), δ 33.80 (s, 1P). MS (FAB, ^{192}Os): m/z 866 $(M)^+$; anal. calcd for $C_{32}H_{30}F_6N_6OsP_2$: N, 9.72; C, 44.44; H, 3.50. Found: N, 9.36; C, 43.99; H, 3.76.

Selected crystal data of 3

$C_{35}H_{37}F_6N_6OsP_2$; M = 907.85; monoclinic; space group = $C2/c$; a = 23.1156(7) Å, b = 16.4313(5) Å, c = 18.4153(5) Å, β = 96.193(2)°, V = 6953.7(4) Å^3; Z = 8; ρ_{calcd} = 1.734 Mg m^{-3}; F(000) = 3592; crystal size = 0.20 × 0.15 × 0.03 mm^3; λ(Mo-K$_\alpha$) = 0.71073 Å; T = 150(2) K; μ = 3.828 mm^{-1}; 23 283 reflections collected, 7950 independent reflections (R_{int} = 0.0554), GOF = 1.056, final $R_1[I > 2\sigma(I)]$ = 0.0482 and wR_2 (all data) = 0.1409.

Preparation of 4

Similar to the procedure described for **3**, this reaction was conducted using $Os_3(CO)_{12}$ (100 mg, 0.11 mmol), $bipzH_2$ (93 mg, 0.34 mmol), 1,10-phenanthroline (61 mg, 0.34 mmol), Me_3NO (52 mg, 0.69 mmol) and pp2b (91 mg, 0.36 mmol), giving a dark-brown crystalline solid (105 mg, 0.12 mmol) in 35% yield.

Spectroscopic data of 4

^{1}H NMR (400 MHz, d_6-acetone, 294 K): δ 9.09 (d, J = 5.2 Hz, 1H), 8.44 (m, 2H), 8.04 (m, 3H), 7.93 (t, J = 7.2 Hz, 1H), 7.76 (m, 2H), 7.52 (m, 3H), 6.59 (s, 1H), 6.38 (s, 1H), 3.71 (m, 1H), 2.67 (m, 2H), 2.14 (m, 1H), 1.90 (m, 2H), 1.63 (m, 2H), 1.20 (m, 4H), 0.82 (m, 3H), 0.21 (m, 1H); ^{19}F–{^{1}H} NMR (470 MHz, d_6-acetone, 294 K): δ −59.51 (s, 3F), −59.69 (s, 3F); ^{31}P NMR (202 MHz, d_6-acetone, 298 K): δ 39.13 (s, 1P), 33.53 (s, 1P). MS (FAB, ^{192}Os): m/z 890 $(M)^+$; anal. calcd for $C_{34}H_{30}F_6N_6OsP_2$: N, 9.46; C, 45.94; H, 3.40. Found: N, 9.23; C, 45.98; H, 3.95.

Preparations of 5 and 6

The Os(II) complexes **5** and **6** were obtained in 21% and 27% yields respectively using similar procedures as described for the preparation of **4**.

Spectroscopic data of 5

^{1}H NMR (400 MHz, d_6-acetone, 294 K): δ 8.83 (s, 1H), 8.21 (q, J = 9.6 Hz, 2H), 7.91 (t, J = 6.8 Hz, 1H), 7.74 (t, J = 6.8 Hz, 1H), 7.64 (d, J = 2.8 Hz, 2H), 7.44 (m, 2H), 6.57 (s, 1H), 6.38 (s, 1H), 3.73–3.65 (m, 1H), 2.73–2.63 (m, 8H), 2.39 (s, 3H), 2.31 (s, 3H), 2.18–2.11 (m, 1H), 1.96–1.82 (m, 2H), 1.73–1.63 (m, 3H), 1.28–1.13 (m, 3H), 1.03–0.93 (m, 1H), 0.86–0.75 (m, 2H), 0.27–0.20 (m, 1H); ^{19}F–{^{1}H} NMR (470 MHz, d_6-acetone, 294 K): δ −59.42 (s, 3F), −59.68 (s, 3F); ^{31}P NMR (202 MHz, d_6-acetone, 298 K): δ 38.81 (s, 1P), 33.74 (s, 1P). MS (FAB, ^{192}Os): m/z 946 $(M)^+$; anal. calcd for $C_{38}H_{38}F_6N_6OsP_2$: N, 8.89; C, 48.30; H, 4.05. Found: N, 9.12; C, 48.37; H, 4.28.

Spectroscopic data of 6

^{1}H NMR (400 MHz, d_6-acetone, 294 K): δ 9.19 (d, J = 5.6 Hz, 1H), 8.17–8.08 (m, 3H), 7.95 (t, J = 6.8 Hz, 1H), 7.80–7.76 (m, 2H), 7.70–7.52 (m, 13H), 6.61 (s, 1H), 6.42 (s, 1H), 3.813.74 (m, 1H), 2.74–2.70 (m, 2H), 2.23–2.12 (m, 1H), 1.99–1.86 (m, 1H), 1.77–1.51 (m, 3H), 1.36–1.14 (m, 4H), 0.97–0.77 (m, 3H), 0.46–0.32 (m, 1H); ^{19}F–{^{1}H} NMR (470 MHz, d_6-acetone, 294 K): δ −59.59 (s, 3F), −59.61 (s, 3F); ^{31}P NMR (202 MHz, d_6-acetone, 298 K): δ 38.93 (s, 1P), 33.89 (s, 1P). MS (FAB, ^{192}Os): m/z 1042 $(M)^+$; anal. calcd for $C_{46}H_{38}F_6N_6OsP_2$: N, 8.07; C, 53.07; H, 3.68. Found: N, 7.99; C, 52.58; H, 3.90.

Single crystal X-ray diffraction studies

Single crystal X-ray diffraction studies were carried out on a Bruker SMART Apex CCD diffractometer using (Mo-K_α) radiation (λ = 0.71073 Å). The data collection was executed using the SMART program. Cell refinement and data reduction were performed using the SAINT program. The structure was determined using the SHELXTL/PC program and refined using full-matrix least squares. CCDC 1044312 and 1044313.

Computational methods

All the calculations were performed using the Gaussian 09 program package, with the B3LYP functional[79,80] and the LANL2DZ[81] basis set for Os and 6-31G**[82] for all other atoms. A conductor-like polarization continuum model CPCM of CH_2Cl_2 solvent was applied to all calculations, and the results were analyzed further using GaussSum.[83] Structures obtained were confirmed as true minima by the absence of imaginary frequencies.

OLED fabrication

All commercial materials and ITO-coated glass were purchased from Nichem and Lumtec. Before thermal evaporation, materials were subjected to temperature-gradient sublimation under high vacuum ($\sim 10^{-6}$ Torr). The bottom-emitting OLED architecture consists of multiple organic layers and a reflective cathode which were consecutively deposited onto the ITO-coated glass substrate. The deposition rates of organics and aluminum were kept at $\sim$0.1 nm s^{-1} and 0.5 nm s^{-1}, respectively. The active area was defined by the shadow mask (2 × 2 mm^2). The measurement of EL characteristics was conducted in a glove box filled with nitrogen. Current density–voltage–luminance characterization was measured using a Keithley 238 current source-measure unit and a Keithley 6485 picoammeter equipped with a calibrated Si-photodiode. The electroluminescence spectra were recorded using an Ocean Optics spectrometer.

Acknowledgements

This work was supported by the Ministry of Science and Technology of Taiwan, under the grant numbers 101-2113-M-007-013-MY3 and 102-2221-E-155-080-MY3. P.J.L. gratefully acknowledges support from the Australian Research Council and the award of a Future Fellowship [FT120100073].

References

1 R. C. Evans, P. Douglas and C. J. Winscom, *Coord. Chem. Rev.*, 2006, **250**, 2093.
2 P.-T. Chou and Y. Chi, *Chem. – Eur. J.*, 2007, **13**, 380.
3 J. A. G. Williams, S. Develay, D. L. Rochester and L. Murphy, *Coord. Chem. Rev.*, 2008, **252**, 2596.
4 A. F. Rausch, M. E. Thompson and H. Yersin, *J. Phys. Chem. A*, 2009, **113**, 5927.
5 A. F. Rausch, H. H. H. Homeier and H. Yersin, *Top. Organomet. Chem.*, 2010, **29**, 193.
6 Y. Chi and P.-T. Chou, *Chem. Soc. Rev.*, 2010, **39**, 638.
7 P.-T. Chou, Y. Chi, M.-W. Chung and C.-C. Lin, *Coord. Chem. Rev.*, 2011, **255**, 2653.
8 J. Kalinowski, V. Fattori, M. Cocchi and J. A. G. Williams, *Coord. Chem. Rev.*, 2011, **255**, 2401.
9 Y. Chi, B. Tong and P.-T. Chou, *Coord. Chem. Rev.*, 2014, **281**, 1–25.
10 Y. You and S. Y. Park, *Dalton Trans.*, 2009, 1267.
11 G. Zhou, W.-Y. Wong and S. Suo, *J. Photochem. Photobiol., C*, 2010, **11**, 133.
12 L. Xiao, Z. Chen, B. Qu, J. Luo, S. Kong, Q. Gong and J. Kido, *Adv. Mater.*, 2011, **23**, 926.
13 H. Sasabe and J. Kido, *Eur. J. Org. Chem.*, 2013, 7653.
14 B. D'Andrade, *Nat. Photonics*, 2007, **1**, 33.
15 K. T. Kamtekar, A. P. Monkman and M. R. Bryce, *Adv. Mater.*, 2010, **22**, 572.
16 M. C. Gather, A. Koehnen and K. Meerholz, *Adv. Mater.*, 2011, **23**, 233.
17 H. Sasabe and J. Kido, *J. Mater. Chem. C*, 2013, **1**, 1699.
18 Y.-L. Chang and Z.-H. Lu, *J. Disp. Technol.*, 2013, **9**, 459.
19 J. Chen, F. Zhao and D. Ma, *Mater. Today*, 2014, **17**, 175.
20 W. Kaim, *Coord. Chem. Rev.*, 2011, **255**, 2503.
21 V. J. Pansare, S. Hejazi, W. J. Faenza and R. K. Prud'homme, *Chem. Mater.*, 2012, **24**, 812.
22 H. Xiang, J. Cheng, X. Ma, X. Zhou and J. J. Chruma, *Chem. Soc. Rev.*, 2013, **42**, 6128.
23 M. A. Bennett, S. K. Bhargava, E. C.-C. Cheng, W. H. Lam, T. K.-M. Lee, S. H. Priver, J. Wagler, A. C. Willis and V. W.-W. Yam, *J. Am. Chem. Soc.*, 2010, **132**, 7094.
24 E. Rossi, L. Murphy, P. L. Brothwood, A. Colombo, C. Dragonetti, D. Roberto, R. Ugo, M. Cocchi and J. A. G. Williams, *J. Mater. Chem.*, 2011, **21**, 15501.

25 M.-H. Nguyen and J. H. K. Yip, *Organometallics*, 2011, **30**, 6383.
26 X. Wu, Y. Liu, Y. Wang, L. Wang, H. Tan, M. Zhu, W. Zhu and Y. Cao, *Org. Electron.*, 2012, **13**, 932–937.
27 Y. Zems, A. G. Moiseev and D. F. Perepichka, *Org. Lett.*, 2013, **15**, 5330.
28 Y. Sun, C. Borek, K. Hanson, P. I. Djurovich, M. E. Thompson, J. Brooks, J. J. Brown and S. R. Forrest, *Appl. Phys. Lett.*, 2007, **90**, 213503.
29 K. R. Graham, Y. Yang, J. R. Sommer, A. H. Shelton, K. S. Schanze, J. Xue and J. R. Reynolds, *Chem. Mater.*, 2011, **23**, 5305.
30 A. Damas, M. P. Gullo, M. N. Rager, A. Jutand, A. Barbieri and H. Amouri, *Chem. Commun.*, 2013, **49**, 3796–3798.
31 E. L. Williams, J. Li and G. E. Jabbour, *Appl. Phys. Lett.*, 2006, **89**, 083506.
32 H.-Y. Chen, C.-H. Yang, Y. Chi, Y.-M. Cheng, Y.-S. Yeh, P.-T. Chou, H.-Y. Hsieh, C.-S. Liu, S.-M. Peng and G.-H. Lee, *Can. J. Chem.*, 2006, **84**, 309.
33 R. Tao, J. Qiao, G. Zhang, L. Duan, L. Wang and Y. Qiu, *J. Phys. Chem. C*, 2012, **116**, 11658.
34 X. Cao, J. Miao, M. Zhu, C. Zhong, C. Yang, H. Wu, J. Qin and Y. Cao, *Chem. Mater.*, 2015, **27**, 96–104.
35 M. Schulze, A. Steffen and F. Würthner, *Angew. Chem., Int. Ed.*, 2015, **54**, 1570.
36 T.-C. Lee, J.-Y. Hung, Y. Chi, Y.-M. Cheng, G.-H. Lee, P.-T. Chou, C.-C. Chen, C.-H. Chang and C.-C. Wu, *Adv. Funct. Mater.*, 2009, **19**, 2639.
37 B.-S. Du, J.-L. Liao, M.-H. Huang, C.-H. Lin, H.-W. Lin, Y. Chi, H.-A. Pan, G.-L. Fan, K.-T. Wong, G.-H. Lee and P.-T. Chou, *Adv. Funct. Mater.*, 2012, **22**, 3491.
38 J.-L. Liao, Y. Chi, S.-H. Liu, G.-H. Lee, P.-T. Chou, H.-X. Huang, Y.-D. Su, C.-H. Chang, J.-S. Lin and M.-R. Tseng, *Inorg. Chem.*, 2014, **53**, 9366.
39 P.-C. Wu, J.-K. Yu, Y.-H. Song, Y. Chi, P.-T. Chou, S.-M. Peng and G.-H. Lee, *Organometallics*, 2003, **22**, 4938.
40 Y.-L. Tung, P.-C. Wu, C.-S. Liu, Y. Chi, J.-K. Yu, Y.-H. Hu, P.-T. Chou, S.-M. Peng, G.-H. Lee, Y. Tao, A. J. Carty, C.-F. Shu and F.-I. Wu, *Organometallics*, 2004, **23**, 3745.
41 F.-C. Hsu, Y.-L. Tung, Y. Chi, C.-C. Hsu, Y.-M. Cheng, M.-L. Ho, P.-T. Chou, S.-M. Peng and A. J. Carty, *Inorg. Chem.*, 2006, **45**, 10188.
42 S.-H. Chang, C.-F. Chang, J.-L. Liao, Y. Chi, D.-Y. Zhou, L.-S. Liao, T.-Y. Jiang, T.-P. Chou, E. Y. Li, G.-H. Lee, T.-Y. Kuo and P.-T. Chou, *Inorg. Chem.*, 2013, **52**, 5867.
43 J.-L. Liao, Y. Chi, Y.-D. Su, H.-X. Huang, C.-H. Chang, S.-H. Liu, G.-H. Lee and P.-T. Chou, *J. Mater. Chem. C*, 2014, **2**, 6269.
44 Y.-M. Cheng, G.-H. Lee, P.-T. Chou, L.-S. Chen, Y. Chi, C.-H. Yang, Y.-H. Song, S.-Y. Chang, P.-I. Shih and C.-F. Shu, *Adv. Funct. Mater.*, 2008, **18**, 183.
45 S. Joerg, R. S. Drago and J. Sales, *Organometallics*, 1998, **17**, 589.
46 S.-W. Li, Y.-M. Cheng, Y.-S. Yeh, C.-C. Hsu, P.-T. Chou, S.-M. Peng, G.-H. Lee, Y.-L. Tung, P.-C. Wu, Y. Chi, F.-I. Wu and C.-F. Shu, *Chem. – Eur. J.*, 2005, **11**, 6347.
47 L.-M. Huang, G.-M. Tu, Y. Chi, W.-Y. Hung, Y.-C. Song, M.-R. Tseng, P.-T. Chou, G.-H. Lee, K.-T. Wong, S.-H. Cheng and W.-S. Tsai, *J. Mater. Chem. C*, 2013, **1**, 7582.
48 H.-Y. Ku, B. Tong, Y. Chi, H.-C. Kao, C.-C. Yeh, C.-H. Chang and G.-H. Lee, *Dalton Trans.*, 2015, DOI: 10.1039/C1034DT03028A.
49 E. M. Kober, J. L. Marshall, W. J. Dressick, B. P. Sullivan, J. V. Caspar and T. J. Meyer, *Inorg. Chem.*, 1985, **24**, 2755–2763.
50 E. M. Kober, J. V. Caspar, R. S. Lumpkin and T. J. Meyer, *J. Phys. Chem.*, 1986, **90**, 3722.
51 M. V. Werrett, D. Chartrand, J. D. Gale, G. S. Hanan, J. G. MacLellan, M. Massi, S. Muzzioli, P. Raiteri, B. W. Skelton, M. Silberstein and S. Stagni, *Inorg. Chem.*, 2011, **50**, 1229.
52 K. P. S. Zanoni, B. K. Kariyazaki, A. Ito, M. K. Brennaman, T. J. Meyer and N. Y. Murakami Iha, *Inorg. Chem.*, 2014, **53**, 4089.
53 B. Carlson, G. D. Phelan, W. Kaminsky, L. Dalton, X. Z. Jiang, S. Liu and A. K.-Y. Jen, *J. Am. Chem. Soc.*, 2002, **124**, 14162.
54 J. V. Caspar, T. D. Westmoreland, G. H. Allen, P. G. Bradley, T. J. Meyer and W. H. Woodruff, *J. Am. Chem. Soc.*, 1984, **106**, 3492.
55 J. A. Treadway, B. Loeb, R. Lopez, P. A. Anderson, F. R. Keene and T. J. Meyer, *Inorg. Chem.*, 1996, **35**, 2242.
56 N. H. Damrauer, T. R. Boussie, M. Devenney and J. K. McCusker, *J. Am. Chem. Soc.*, 1997, **119**, 8253.
57 K. E. Spettel and N. H. Damrauer, *J. Phys. Chem. A*, 2014, **118**, 10649.
58 P. C. Alford, M. J. Cook, A. P. Lewis, G. S. G. McAuliffe, V. Skarda, A. J. Thomson, J. L. Glasper and D. J. Robbins, *J. Chem. Soc., Perkin Trans. 2*, 1985, 705.
59 Y.-L. Chen, S.-W. Lee, Y. Chi, K.-C. Hwang, S. B. Kumar, Y.-H. Hu, Y.-M. Cheng, P.-T. Chou, S.-M. Peng, G.-H. Lee, S.-J. Yeh and C.-T. Chen, *Inorg. Chem.*, 2005, **44**, 4287.
60 Z. Deng, S. T. Lee, D. P. Webb, Y. C. Chan and W. A. Gambling, *Synth. Met.*, 1999, **107**, 107–109.
61 S.-J. Su, D. Tanaka, Y.-J. Li, H. Sasabe, T. Takeda and J. Kido, *Org. Lett.*, 2008, **10**, 941.
62 A. Endo, K. Sato, K. Yoshimura, T. Kai, A. Kawada, H. Miyazaki and C. Adachi, *Appl. Phys. Lett.*, 2011, **98**, 083302.
63 C.-H. Chang, C.-L. Ho, Y.-S. Chang, I.-C. Lien, C.-H. Lin, Y.-W. Yang, J.-L. Liao and Y. Chi, *J. Mater. Chem. C*, 2013, **1**, 2639.
64 Y. Hamada, H. Kanno, T. Tsujioka, H. Takahashi and T. Usuki, *Appl. Phys. Lett.*, 1999, **75**, 1682.
65 S. C. Tse, K. C. Kwok and S. K. So, *Appl. Phys. Lett.*, 2006, **89**, 262102.
66 J. Lee, J.-I. Lee, K.-I. Song, S. J. Lee and H. Y. Chu, *Appl. Phys. Lett.*, 2008, **92**, 133304.
67 Y.-L. Tung, S.-W. Lee, Y. Chi, Y.-T. Tao, C.-H. Chien, Y.-M. Cheng, P.-T. Chou, S.-M. Peng and C.-S. Liu, *J. Mater. Chem.*, 2005, **15**, 460.
68 T.-H. Liu, S.-F. Hsu, M.-H. Ho, C.-H. Liao, Y.-S. Wu, C. H. Chen, Y.-L. Tung, P.-C. Wu and Y. Chi, *Appl. Phys. Lett.*, 2006, **88**, 063508.

69 C.-H. Chien, F.-M. Hsu, C.-F. Shu and Y. Chi, *Org. Electron.*, 2009, **10**, 871.
70 J. Kalinowski, M. Cocchi, V. Fattori, L. Murphy and J. A. G. Williams, *Org. Electron.*, 2010, **11**, 724–730.
71 S.-J. Su, E. Gonmori, H. Sasabe and J. Kido, *Adv. Mater.*, 2008, **20**, 4189.
72 H. Sasabe, J.-i. Takamatsu, T. Motoyama, S. Watanabe, G. Wagenblast, N. Langer, O. Molt, E. Fuchs, C. Lennartz and J. Kido, *Adv. Mater.*, 2010, **22**, 5003.
73 M. A. Baldo, C. Adachi and S. R. Forrest, *Phys. Rev. B: Condens. Matter Mater. Phys.*, 2000, **62**, 10967.
74 D. Hertel and K. Meerholz, *J. Phys. Chem. B*, 2007, **111**, 12075.
75 S. Reineke, K. Walzer and K. Leo, *Phys. Rev. B: Condens. Matter Mater. Phys.*, 2007, **75**, 125328.
76 H.-H. Yeh, S.-T. Ho, Y. Chi, J. N. Clifford, E. Palomares, S.-H. Liu and P.-T. Chou, *J. Mater. Chem. A*, 2013, **1**, 7681.
77 L. Porrès, A. Holland, L.-O. Pålsson, A. Monkman, C. Kemp and A. Beeby, *J. Fluoresc.*, 2006, **16**, 267–273.
78 A. K. Gaigalas and L. Wang, *J. Res. Natl. Inst. Stand. Technol.*, 2008, **113**, 17.
79 A. D. Becke, *J. Chem. Phys.*, 1993, **98**, 5648.
80 P. J. Stephens, F. J. Devlin, C. F. Chabalowski and M. J. Frisch, *J. Phys. Chem.*, 1994, **98**, 11623–11627.
81 P. J. Hay and W. R. Wadt, *J. Chem. Phys.*, 1985, **82**, 299.
82 G. A. Petersson and M. A. Al-Laham, *J. Chem. Phys.*, 1991, **94**, 6081.
83 N. M. O'Boyle, A. L. Tenderholt and K. M. Langner, *J. Comput. Chem.*, 2008, **29**, 839.

